

Convolutional Approximations to the General Non-Line-of-Sight Imaging Operator: Supplemental Material

Byeongjoo Ahn¹ Akshat Dave² Ashok Veeraraghavan²
Ioannis Gkioulekas¹ Aswin C. Sankaranarayanan¹

¹Carnegie Mellon University ²Rice University

1. Introduction

In this supplemental material, we cover the following topics:

1. In Section 2, we provide supplementary derivations of our convolutional approximations for alternative backprojection and conventional backprojection, and backprojection with confocal light transients. Additionally, we prove the linear least-squares problem with the Gram operator provides the same solution with the original least-squares problem. Finally, we provide the algorithmic details of using ADMM for our reconstruction.
2. In Section 3, we provide more details about the hardware prototype, calibration and acquisition procedures.
3. In Section 4, we provide the implementation detail, the geometric parameters for each NLOS scene, and the additional results in the main paper from various viewpoints.

2. Supplementary Derivations

We provide detailed derivations of our convolutional model in the Proposition 1, and the algorithmic details of our reconstruction techniques.

2.1. Convolutional approximations

We derive the convolutional model for the two definitions of backprojections introduced in the main paper — first, the alternative backprojection $\rho_{\text{bp,alt}}$ which is simpler, and then the backprojection ρ_{bp} . Basic setup is shown in Figure 1. Our proof is based on the fact that, assuming an infinite LOS surface, every NLOS point has its corresponding set of illumination and sensing points where the ellipsoids have the same tangent planes as shown in Figure 2.

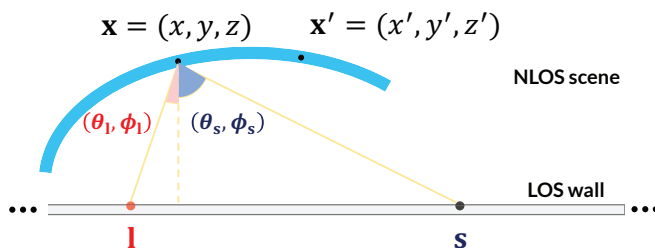


Figure 1. Notations for the derivation.

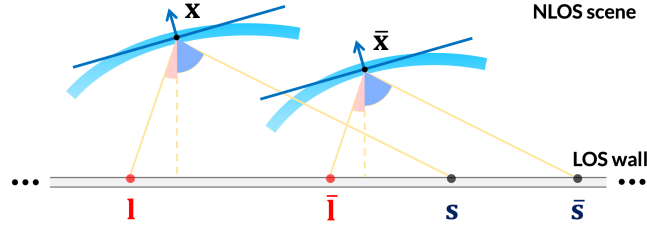


Figure 2. **Same set of ellipsoids.** If we assume an infinite LOS wall, every NLOS point has its corresponding set of illumination and sensing points where the ellipsoids have the same tangent planes. Thus, the kernel, which is the weighted superposition of ellipsoids, becomes spatially invariant (after the normalization to compensate the light fall-off).

2.1.1 Alternative backprojection.

In alternative definitions of backprojection, *i.e.*, $(\mathbf{A} > 0)^\top$ operation, we backproject the intensity of light transient without light fall-off terms. It can be expressed as follows:

$$\begin{aligned}
 \rho_{\text{bp,alt}}(\mathbf{x}') &= \iiint_{\Omega_{\mathbf{l},\mathbf{s},t}} i(t; \mathbf{l}, \mathbf{s}) \delta(ct - \|\mathbf{x}' - \mathbf{l}\| - \|\mathbf{x}' - \mathbf{s}\|) dt ds d\mathbf{l} \\
 &= \iiint_{\Omega_{\mathbf{l},\mathbf{s},t}} \left(\iiint_{\Omega_{\mathbf{x}}} \rho(\mathbf{x}) \frac{\delta(\|\mathbf{x} - \mathbf{l}\| + \|\mathbf{x} - \mathbf{s}\| - ct)}{\|\mathbf{x} - \mathbf{l}\|^2 \|\mathbf{x} - \mathbf{s}\|^2} d\mathbf{x} \right) \delta(ct - \|\mathbf{x}' - \mathbf{l}\| - \|\mathbf{x}' - \mathbf{s}\|) dt ds d\mathbf{l} \\
 &= \iiint_{\Omega_{\mathbf{x}}} \rho(\mathbf{x}) \iiint_{\Omega_{\mathbf{l},\mathbf{s},t}} \frac{\delta(\|\mathbf{x} - \mathbf{l}\| + \|\mathbf{x} - \mathbf{s}\| - ct) \delta(ct - \|\mathbf{x}' - \mathbf{l}\| - \|\mathbf{x}' - \mathbf{s}\|)}{\|\mathbf{x} - \mathbf{l}\|^2 \|\mathbf{x} - \mathbf{s}\|^2} dt ds d\mathbf{l} d\mathbf{x} \\
 &= \iiint_{\Omega_{\mathbf{x}}} \rho(\mathbf{x}) k_{\text{alt}}(\mathbf{x}, \mathbf{x}') d\mathbf{x},
 \end{aligned} \tag{1}$$

where the notation is the same as the main paper that i is 5D light transient, ρ is the NLOS albedo, \mathbf{l} and \mathbf{s} are illumination point and sensing point on the LOS wall, \mathbf{x} and \mathbf{x}' are the points at NLOS scene, t is time, and c is the speed of light.

When the size of LOS wall is infinite, $k_{\text{alt}}(\mathbf{x}, \mathbf{x}')$ can be expressed as $k_{\text{alt}}(\mathbf{x}' - \mathbf{x})$ for \mathbf{x}' in close vicinity to \mathbf{x} as follows:

$$\begin{aligned}
k_{\text{alt}}(\mathbf{x}, \mathbf{x}') &= \iiint_{\Omega_{1,s,t}} \frac{\delta(\|\mathbf{x} - \mathbf{l}\| + \|\mathbf{x} - \mathbf{s}\| - ct) \delta(ct - \|\mathbf{x}' - \mathbf{l}\| - \|\mathbf{x}' - \mathbf{s}\|)}{\|\mathbf{x} - \mathbf{l}\|^2 \|\mathbf{x} - \mathbf{s}\|^2} dt ds d\mathbf{l} \\
&= \frac{1}{c} \iiint_{\Omega_{1,s}} \frac{\delta(\|\mathbf{x}' - \mathbf{l}\| + \|\mathbf{x}' - \mathbf{s}\| - \|\mathbf{x} - \mathbf{l}\| - \|\mathbf{x} - \mathbf{s}\|)}{\|\mathbf{x} - \mathbf{l}\|^2 \|\mathbf{x} - \mathbf{s}\|^2} ds d\mathbf{l} \\
&\approx \frac{1}{c} \iiint_{\Omega_{1,s}} \frac{\delta\left(\|\mathbf{x} - \mathbf{l}\| + \left\langle \mathbf{x}' - \mathbf{x}, \frac{\mathbf{x} - \mathbf{l}}{\|\mathbf{x} - \mathbf{l}\|} \right\rangle + \|\mathbf{x} - \mathbf{s}\| + \left\langle \mathbf{x}' - \mathbf{x}, \frac{\mathbf{x} - \mathbf{s}}{\|\mathbf{x} - \mathbf{s}\|} \right\rangle - \|\mathbf{x} - \mathbf{l}\| - \|\mathbf{x} - \mathbf{s}\|\right)}{\|\mathbf{x} - \mathbf{l}\|^2 \|\mathbf{x} - \mathbf{s}\|^2} ds d\mathbf{l} \\
&= \frac{1}{c} \iiint_{\Omega_{1,s}} \frac{\delta\left(\left\langle \mathbf{x}' - \mathbf{x}, \frac{\mathbf{x} - \mathbf{l}}{\|\mathbf{x} - \mathbf{l}\|} + \frac{\mathbf{x} - \mathbf{s}}{\|\mathbf{x} - \mathbf{s}\|} \right\rangle\right)}{\|\mathbf{x} - \mathbf{l}\|^2 \|\mathbf{x} - \mathbf{s}\|^2} ds d\mathbf{l} \tag{2} \\
&= \frac{1}{c} \int_{-\pi}^{\pi} \int_0^{\frac{\pi}{2}} \int_{-\pi}^{\pi} \int_0^{\frac{\pi}{2}} \frac{\delta\left(\left\langle \mathbf{x}' - \mathbf{x}, \frac{\mathbf{x} - \mathbf{l}}{\|\mathbf{x} - \mathbf{l}\|} + \frac{\mathbf{x} - \mathbf{s}}{\|\mathbf{x} - \mathbf{s}\|} \right\rangle\right)}{\frac{z^2}{\cos^2 \theta_1} \frac{z^2}{\cos^2 \theta_s}} \frac{z^2 \tan \theta_s}{\cos^2 \theta_s} d\theta_s d\phi_s \frac{z^2 \tan \theta_1}{\cos^2 \theta_1} d\theta_1 d\phi_1 \\
&= \frac{1}{c} \int_{-\pi}^{\pi} \int_0^{\frac{\pi}{2}} \int_{-\pi}^{\pi} \int_0^{\frac{\pi}{2}} \delta(\langle \mathbf{x}' - \mathbf{x}, \mathbf{n}(\theta_1, \theta_s, \phi_1, \phi_s) \rangle) \tan \theta_1 \tan \theta_s d\theta_1 d\theta_s d\phi_1 d\phi_s \\
&= k_{\text{alt}}(\mathbf{x}' - \mathbf{x}),
\end{aligned}$$

where we used the property of Dirac delta function $\int \delta(a - t) \delta(t - b) dt = \delta(b - a)$ in the second line, and the first-order approximation of $\|\cdot\|_2$ because of \mathbf{x}' in close vicinity to \mathbf{x} in the third line. The vector $(\mathbf{x} - \mathbf{l})$ and $(\mathbf{x} - \mathbf{s})$ are parameterized by the depth z and the angle (θ_1, ϕ_1) , (θ_s, ϕ_s) ; when $\mathbf{x} = (x, y, z)$ and the LOS wall is $z = 0$, it is parameterized as $(\mathbf{x} - \mathbf{l}) = (z \tan \theta_1 \cos \phi_1, z \tan \theta_1 \sin \phi_1, z)$ and $(\mathbf{x} - \mathbf{s}) = (z \tan \theta_s \cos \phi_s, z \tan \theta_s \sin \phi_s, z)$.

The normal vector \mathbf{n} corresponds to the normal of the ellipsoid determined by \mathbf{l} and \mathbf{s} at the NLOS point \mathbf{x} , and is the function of $(\theta_1, \theta_s, \phi_1, \phi_s)$. Since the size of LOS wall is infinite, the range of integral for $\theta_1, \theta_s, \phi_1, \phi_s$ is the same for every \mathbf{x} and \mathbf{x}' (i.e., $\theta_1, \theta_s \in [0, \frac{\pi}{2}]$, $\phi_1, \phi_s \in [-\pi, \pi]$). Thus, the effect of angles is canceled out after the integration and the kernel becomes the function of only $\mathbf{x}' - \mathbf{x}$, which makes (1) the convolutional form as follows:

$$\begin{aligned}
\therefore \rho_{\text{bp,alt}}(\mathbf{x}') &= \iiint_{\Omega_{\mathbf{x}}} \rho(\mathbf{x}) k_{\text{alt}}(\mathbf{x}, \mathbf{x}') d\mathbf{x} \\
&= \iiint_{\Omega_{\mathbf{x}}} \rho(\mathbf{x}) k_{\text{alt}}(\mathbf{x}' - \mathbf{x}) d\mathbf{x} \tag{3} \\
&= (\rho * k_{\text{alt}})(\mathbf{x}').
\end{aligned}$$

Upon discretization, it can be expressed as

$$\rho_{\text{bp,alt}} = (\mathbf{A} > 0)^\top \mathbf{A} \boldsymbol{\rho} = \mathbf{k}_{\text{alt}} * \boldsymbol{\rho}. \tag{4}$$

2.1.2 Conventional backprojection.

In the conventional definition of backprojection, *i.e.*, \mathbf{A}^\top operation, we backproject the intensity of light transient while including the light fall-off terms. It can be expressed as follows:

$$\begin{aligned}
\rho_{\text{bp}}(\mathbf{x}') &= \iiint_{\Omega_{1,s,t}} i(t; \mathbf{l}, \mathbf{s}) \frac{\delta(ct - \|\mathbf{x}' - \mathbf{l}\| - \|\mathbf{x}' - \mathbf{s}\|)}{\|\mathbf{x}' - \mathbf{l}\|^2 \|\mathbf{x}' - \mathbf{s}\|^2} dt ds d\mathbf{l} \\
&= \iiint_{\Omega_{1,s,t}} \left(\iiint_{\Omega_{\mathbf{x}}} \rho(\mathbf{x}) \frac{\delta(\|\mathbf{x} - \mathbf{l}\| + \|\mathbf{x} - \mathbf{s}\| - ct)}{\|\mathbf{x} - \mathbf{l}\|^2 \|\mathbf{x} - \mathbf{s}\|^2} d\mathbf{x} \right) \frac{\delta(ct - \|\mathbf{x}' - \mathbf{l}\| - \|\mathbf{x}' - \mathbf{s}\|)}{\|\mathbf{x}' - \mathbf{l}\|^2 \|\mathbf{x}' - \mathbf{s}\|^2} dt ds d\mathbf{l} \\
&= \iiint_{\Omega_{\mathbf{x}}} \rho(\mathbf{x}) \iiint_{\Omega_{1,s,t}} \frac{\delta(\|\mathbf{x} - \mathbf{l}\| + \|\mathbf{x} - \mathbf{s}\| - ct) \delta(ct - \|\mathbf{x}' - \mathbf{l}\| - \|\mathbf{x}' - \mathbf{s}\|)}{\|\mathbf{x} - \mathbf{l}\|^2 \|\mathbf{x} - \mathbf{s}\|^2 \|\mathbf{x}' - \mathbf{l}\|^2 \|\mathbf{x}' - \mathbf{s}\|^2} dt ds d\mathbf{l} d\mathbf{x} \\
&= \iiint_{\Omega_{\mathbf{x}}} \rho(\mathbf{x}) k(\mathbf{x}, \mathbf{x}') d\mathbf{x},
\end{aligned} \tag{5}$$

where everything is the same with (1) except the additional light fall-off term $\frac{1}{\|\mathbf{x}' - \mathbf{l}\|^2 \|\mathbf{x}' - \mathbf{s}\|^2}$. Similarly, for \mathbf{x}' in close vicinity to \mathbf{x} , the kernel $k(\mathbf{x}, \mathbf{x}')$ can also be expressed as $k(\mathbf{x}' - \mathbf{x})$ as follows:

$$\begin{aligned}
k(\mathbf{x}, \mathbf{x}') &= \iiint_{\Omega_{1,s,t}} \frac{\delta(\|\mathbf{x} - \mathbf{l}\| + \|\mathbf{x} - \mathbf{s}\| - ct) \delta(ct - \|\mathbf{x}' - \mathbf{l}\| - \|\mathbf{x}' - \mathbf{s}\|)}{\|\mathbf{x} - \mathbf{l}\|^2 \|\mathbf{x} - \mathbf{s}\|^2 \|\mathbf{x}' - \mathbf{l}\|^2 \|\mathbf{x}' - \mathbf{s}\|^2} dt ds d\mathbf{l} \\
&= \frac{1}{c} \iiint_{\Omega_{1,s}} \frac{\delta(\|\mathbf{x}' - \mathbf{l}\| + \|\mathbf{x}' - \mathbf{s}\| - \|\mathbf{x} - \mathbf{l}\| - \|\mathbf{x} - \mathbf{s}\|)}{\|\mathbf{x} - \mathbf{l}\|^2 \|\mathbf{x} - \mathbf{s}\|^2 \|\mathbf{x}' - \mathbf{l}\|^2 \|\mathbf{x}' - \mathbf{s}\|^2} ds d\mathbf{l} \\
&\approx \frac{1}{c} \iiint_{\Omega_{1,s}} \frac{\delta\left(\|\mathbf{x} - \mathbf{l}\| + \left\langle \mathbf{x}' - \mathbf{x}, \frac{\mathbf{x} - \mathbf{l}}{\|\mathbf{x} - \mathbf{l}\|} \right\rangle + \|\mathbf{x} - \mathbf{s}\| + \left\langle \mathbf{x}' - \mathbf{x}, \frac{\mathbf{x} - \mathbf{s}}{\|\mathbf{x} - \mathbf{s}\|} \right\rangle - \|\mathbf{x} - \mathbf{l}\| - \|\mathbf{x} - \mathbf{s}\|\right)}{\|\mathbf{x} - \mathbf{l}\|^4 \|\mathbf{x} - \mathbf{s}\|^4} ds d\mathbf{l} \\
&= \frac{1}{c} \iiint_{\Omega_{1,s}} \frac{\delta\left(\left\langle \mathbf{x}' - \mathbf{x}, \frac{\mathbf{x} - \mathbf{l}}{\|\mathbf{x} - \mathbf{l}\|} + \frac{\mathbf{x} - \mathbf{s}}{\|\mathbf{x} - \mathbf{s}\|} \right\rangle\right)}{\|\mathbf{x} - \mathbf{l}\|^4 \|\mathbf{x} - \mathbf{s}\|^4} ds d\mathbf{l} \\
&= \frac{1}{c} \int_{-\pi}^{\pi} \int_0^{\frac{\pi}{2}} \int_{-\pi}^{\pi} \int_0^{\frac{\pi}{2}} \frac{\delta\left(\left\langle \mathbf{x}' - \mathbf{x}, \frac{\mathbf{x} - \mathbf{l}}{\|\mathbf{x} - \mathbf{l}\|} + \frac{\mathbf{x} - \mathbf{s}}{\|\mathbf{x} - \mathbf{s}\|} \right\rangle\right)}{\frac{z^4}{\cos^4 \theta_1} \frac{z^4}{\cos^4 \theta_s}} \frac{z^2 \tan \theta_s}{\cos^2 \theta_s} d\theta_s d\phi_s \frac{z^2 \tan \theta_1}{\cos^2 \theta_1} d\theta_1 d\phi_1 \\
&= \frac{1}{z^4} \frac{1}{c} \int_{-\pi}^{\pi} \int_0^{\frac{\pi}{2}} \int_{-\pi}^{\pi} \int_0^{\frac{\pi}{2}} \delta(\langle \mathbf{x}' - \mathbf{x}, \mathbf{n}(\theta_1, \theta_s, \phi_1, \phi_s) \rangle) \sin \theta_1 \cos \theta_1 \sin \theta_s \cos \theta_s d\theta_1 d\theta_s d\phi_1 d\phi_s \\
&= \frac{1}{z^4} f(\mathbf{x}' - \mathbf{x}),
\end{aligned} \tag{6}$$

where f corresponds to the kernel after normalization with z^4 . In the third line, the additional approximation from the vicinity assumption is used; *i.e.*, $\frac{1}{\|\mathbf{x}' - \mathbf{l}\|^2 \|\mathbf{x}' - \mathbf{s}\|^2} \approx \frac{1}{\|\mathbf{x} - \mathbf{l}\|^2 \|\mathbf{x} - \mathbf{s}\|^2}$. Then, (5) becomes the convolutional form as follows:

$$\begin{aligned}
\therefore \rho_{\text{bp}}(\mathbf{x}') &= \iiint_{\Omega_{\mathbf{x}}} \rho(\mathbf{x}) k(\mathbf{x}, \mathbf{x}') d\mathbf{x} \\
&= \iiint_{\Omega_{\mathbf{x}}} \left(\frac{1}{z^4} \rho(\mathbf{x}) \right) f(\mathbf{x}' - \mathbf{x}) d\mathbf{x} \\
&= (\rho_z * f)(\mathbf{x}'). \quad \left(\rho_z(x, y, z) = \frac{1}{z^4} \rho(x, y, z) \right)
\end{aligned} \tag{7}$$

Upon discretization, it can be expressed as

$$\boldsymbol{\rho}_{\text{bp}} = \mathbf{A}^\top \mathbf{A} \boldsymbol{\rho} = \mathbf{f} * (\boldsymbol{\rho}/z^4). \quad (8)$$

2.1.3 Backprojection with confocal light transients.

For confocal light transients, the derivation becomes slightly different as follows:

$$\begin{aligned} k_c(\mathbf{x}, \mathbf{x}') &= \iiint_{\Omega_{1,t}} \frac{\delta(2\|\mathbf{x} - \mathbf{l}\| - ct) \delta(ct - 2\|\mathbf{x}' - \mathbf{l}\|)}{\|\mathbf{x} - \mathbf{l}\|^4 \|\mathbf{x}' - \mathbf{l}\|^4} dt d\mathbf{l} \\ &= \frac{1}{4c} \iint_{\Omega_1} \frac{\delta(\|\mathbf{x}' - \mathbf{l}\| - \|\mathbf{x} - \mathbf{l}\|)}{\|\mathbf{x} - \mathbf{l}\|^4 \|\mathbf{x}' - \mathbf{l}\|^4} d\mathbf{l} \\ &\approx \frac{1}{4c} \iint_{\Omega_1} \frac{\delta\left(\|\mathbf{x} - \mathbf{l}\| + \left\langle \mathbf{x}' - \mathbf{x}, \frac{\mathbf{x} - \mathbf{l}}{\|\mathbf{x} - \mathbf{l}\|} \right\rangle - \|\mathbf{x} - \mathbf{l}\|\right)}{\|\mathbf{x} - \mathbf{l}\|^8} d\mathbf{l} \\ &= \frac{1}{4c} \iint_{\Omega_1} \frac{\delta\left(\left\langle \mathbf{x}' - \mathbf{x}, \frac{\mathbf{x} - \mathbf{l}}{\|\mathbf{x} - \mathbf{l}\|} \right\rangle\right)}{\|\mathbf{x} - \mathbf{l}\|^8} d\mathbf{l} \\ &= \frac{1}{4c} \int_{-\pi}^{\pi} \int_0^{\frac{\pi}{2}} \frac{\delta\left(\left\langle \mathbf{x}' - \mathbf{x}, \frac{\mathbf{x} - \mathbf{l}}{\|\mathbf{x} - \mathbf{l}\|} \right\rangle\right)}{\frac{z^8}{\cos^8 \theta_1}} \frac{z^2 \tan \theta_1}{\cos^2 \theta_1} d\theta_1 d\phi_1 \\ &= \frac{1}{z^6} \frac{1}{4c} \int_{-\pi}^{\pi} \int_0^{\frac{\pi}{2}} \delta(\langle \mathbf{x}' - \mathbf{x}, \mathbf{n}_c(\theta_1, \phi_1) \rangle) \sin \theta_1 \cos^5 \theta_1 d\theta_1 d\phi_1 \\ &= \frac{1}{z^6} f_c(\mathbf{x}' - \mathbf{x}). \end{aligned} \quad (9)$$

The normal vector \mathbf{n}_c corresponds to the normal of the circle determined by \mathbf{l} at the NLOS point \mathbf{x} , *i.e.*, $\frac{\mathbf{x} - \mathbf{l}}{\|\mathbf{x} - \mathbf{l}\|}$, and is the function of (θ_1, ϕ_1) . Similarly with the 5D transient case, the effect of angles is canceled out after the integration and the kernel becomes the function of only $\mathbf{x}' - \mathbf{x}$, and have a convolutional formulation.

2.2. Gram operator

We solve the problem P1:

$$(P1) \quad \hat{\boldsymbol{\rho}} = \underset{\boldsymbol{\rho}}{\operatorname{argmin}} \|\mathbf{i} - \mathbf{A} \boldsymbol{\rho}\|^2, \quad (10)$$

by solving P2:

$$(P2) \quad \hat{\boldsymbol{\rho}} = \underset{\boldsymbol{\rho}}{\operatorname{argmin}} \|\mathbf{A}^\top \mathbf{i} - \mathbf{A}^\top \mathbf{A} \boldsymbol{\rho}\|^2. \quad (11)$$

We provide the proof of this when $\mathbf{A}^\top \mathbf{A}$ is invertible. This is directly derived by the pseudo-inverse of each problem. The pseudo-inverse of (P1) is

$$(P1) \quad \boldsymbol{\rho}^\dagger = (\mathbf{A}^\top \mathbf{A})^{-1} \mathbf{A}^\top \mathbf{i}. \quad (12)$$

If we define $\mathbf{B} = \mathbf{A}^\top \mathbf{A}$, the inverse of (P2) is

$$(P2) \quad \begin{aligned} \boldsymbol{\rho}^\dagger &= \mathbf{B}^{-1} \mathbf{A}^\top \mathbf{i} \\ &= (\mathbf{A}^\top \mathbf{A})^{-1} \mathbf{A}^\top \mathbf{i}. \end{aligned} \quad (13)$$

Thus, we can solve P1 by solving P2 where we can exploit our convolutional model. When we use alternative backprojection, the proof is almost the same for $\mathbf{B} = (\mathbf{A} > 0)^\top \mathbf{A}$ when $(\mathbf{A} > 0)^\top \mathbf{A}$ is invertible.

2.3. Optimization

ADMM update rules. To solve the optimization problem with priors, we use ADMM [1]. For priors, we used non-negativity, sparsity, and total variation (TV). Then, the problem can be expressed as follows:

$$\min_{\boldsymbol{\rho}} \frac{1}{2} \|\boldsymbol{\rho}_{\text{bp}} - \mathbf{A}^\top \mathbf{A} \boldsymbol{\rho}\|^2 + \mathcal{I}_{\mathbb{R}_+}(\boldsymbol{\rho}) + \lambda_1 \|\boldsymbol{\rho}\|_1 + \lambda_{\text{TV}} \|\nabla \boldsymbol{\rho}\|_1. \quad (14)$$

This problem can be rewritten in ADMM form as

$$\begin{aligned} & \text{minimize} \quad \underbrace{\frac{1}{2} \|\boldsymbol{\rho}_{\text{bp}} - \mathbf{z}_1\|^2}_{g_1(\mathbf{z}_1)} + \underbrace{\mathcal{I}_{\mathbb{R}_+}(\mathbf{z}_2)}_{g_2(\mathbf{z}_2)} + \underbrace{\lambda_1 \|\mathbf{z}_3\|_1}_{g_3(\mathbf{z}_3)} + \underbrace{\lambda_{\text{TV}} \|\mathbf{z}_4\|_1}_{g_4(\mathbf{z}_4)} \\ & \text{subject to} \quad \underbrace{\begin{bmatrix} \mathbf{A}^\top \mathbf{A} \\ \mathbf{I} \\ \mathbf{I} \\ \nabla \end{bmatrix}}_{\mathbf{C}} \boldsymbol{\rho} - \underbrace{\begin{bmatrix} \mathbf{z}_1 \\ \mathbf{z}_2 \\ \mathbf{z}_3 \\ \mathbf{z}_4 \end{bmatrix}}_{\mathbf{z}} = \mathbf{0}, \end{aligned} \quad (15)$$

Then, the augmented Lagrangian is as follows:

$$\mathcal{L}_\mu(\boldsymbol{\rho}, \mathbf{z}, \mathbf{y}) = \sum_{i=1}^4 g_i(\mathbf{z}_i) + \mathbf{y}^\top (\mathbf{C} \boldsymbol{\rho} - \mathbf{z}) + \frac{\mu}{2} \|\mathbf{C} \boldsymbol{\rho} - \mathbf{z}\|^2. \quad (16)$$

Using the scaled dual variable $\mathbf{u} = \mathbf{y}/\mu$, we can express ADMM as

$$\begin{aligned}
\mathbf{z}_1 &\leftarrow \underset{\mathbf{z}_1}{\operatorname{argmin}} g_1(\mathbf{z}_1) + \frac{\mu}{2} \|\mathbf{v} - \mathbf{z}_1\|^2, & \mathbf{v} &= \mathbf{A}^\top \mathbf{A} \boldsymbol{\rho} + \mathbf{u}_1 \\
&= \underset{\mathbf{z}_1}{\operatorname{argmin}} \frac{1}{2} \|\boldsymbol{\rho}_{\text{bp}} - \mathbf{z}_1\|^2 + \frac{\mu}{2} \|\mathbf{v} - \mathbf{z}_1\|^2 \\
&= \frac{\boldsymbol{\rho}_{\text{bp}} + \mu \mathbf{v}}{1 + \mu} \\
\mathbf{z}_2 &\leftarrow \underset{\mathbf{z}_2}{\operatorname{argmin}} g_2(\mathbf{z}_2) + \frac{\mu}{2} \|\mathbf{v} - \mathbf{z}_2\|_2^2, & \mathbf{v} &= \boldsymbol{\rho} + \mathbf{u}_2 \\
&= \underset{\mathbf{z}_2}{\operatorname{argmin}} \mathcal{I}_{\mathbb{R}_+}(\mathbf{z}_2) + \frac{\mu}{2} \|\mathbf{v} - \mathbf{z}_2\|_2^2 \\
&= \max(0, \mathbf{v}), \\
\mathbf{z}_3 &\leftarrow \underset{\mathbf{z}_3}{\operatorname{argmin}} g_3(\mathbf{z}_3) + \frac{\mu}{2} \|\mathbf{v} - \mathbf{z}_3\|_2^2, & \mathbf{v} &= \boldsymbol{\rho} + \mathbf{u}_3 \\
&= \underset{\mathbf{z}_3}{\operatorname{argmin}} \lambda_1 \|\mathbf{z}_3\|_1 + \frac{\mu}{2} \|\mathbf{v} - \mathbf{z}_3\|_2^2 \\
&= S_{\lambda_1/\mu}(\mathbf{v}), \\
\mathbf{z}_4 &\leftarrow \underset{\mathbf{z}_4}{\operatorname{argmin}} g_4(\mathbf{z}_4) + \frac{\mu}{2} \|\mathbf{v} - \mathbf{z}_4\|_2^2, & \mathbf{v} &= \nabla \boldsymbol{\rho} + \mathbf{u}_4 \\
&= \underset{\mathbf{z}_4}{\operatorname{argmin}} \lambda_{\text{TV}} \|\mathbf{z}_4\|_1 + \frac{\mu}{2} \|\mathbf{v} - \mathbf{z}_4\|_2^2 \\
&= S_{\lambda_{\text{TV}}/\mu}(\mathbf{v}), \\
\mathbf{u} &\leftarrow \mathbf{u} + \mathbf{C} \boldsymbol{\rho} - \mathbf{z}, \\
\boldsymbol{\rho} &\leftarrow \underset{\boldsymbol{\rho}}{\operatorname{argmin}} \frac{1}{2} \|\mathbf{C} \boldsymbol{\rho} - \mathbf{v}\|_2^2, & \mathbf{v} &= \mathbf{z} - \mathbf{u},
\end{aligned} \tag{17}$$

where S for updating \mathbf{z}_3 and \mathbf{z}_4 denotes soft-thresholding operator.

To update $\boldsymbol{\rho}$, we use gradient descent method because it is computationally demanding to obtain the inverse of \mathbf{C} matrix [4]. Thus, $\boldsymbol{\rho}$ is updated as follows:

$$\boldsymbol{\rho} \leftarrow \boldsymbol{\rho} - \frac{\mu}{\nu} \mathbf{C}^\top (\mathbf{C} \boldsymbol{\rho} - \mathbf{v}), \tag{18}$$

where ν controls the step size of gradient decent approach. We use $\mu = 1$, $\nu = \|\mathbf{C}\|^2 \mu$, $\lambda_1 = 0.05\mu \sim 0.20\mu$, and $\lambda_{\text{TV}} = 0.005\mu \sim 0.010\mu$.

3. Hardware Setup

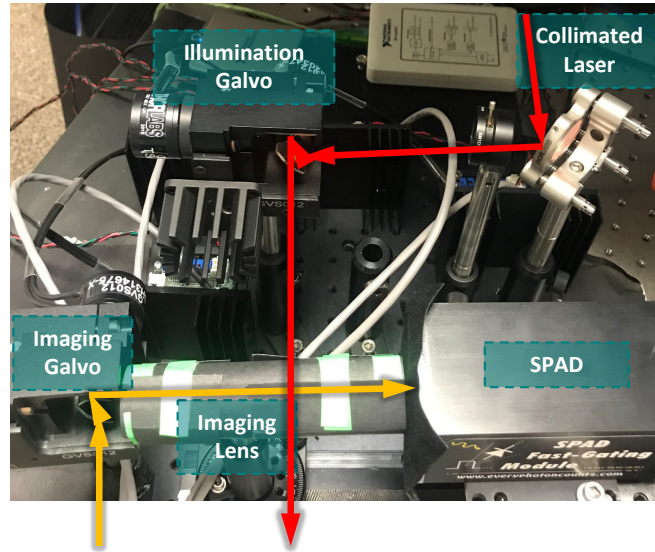


Figure 3. **Hardware prototype.** We build a hardware prototype capable of scanning arbitrary 5D transients by using two galvos to separately steer the illuminated and imaged spots on the wall.

Figure 3 depicts the hardware prototype we have built for acquiring NLOS time-resolved data. The light source is a picosecond pulsed laser with 6 mW average power, 600 nm wavelength, 10 nm bandwidth and 24.9 MHz repetition rate. The colimated beam is steered onto the wall using a 2-axis mirror galvanometer (galvo). The size of the laser spot on the wall is 6 mm and the calibration accuracy for the galvo is 3 mm. A single pixel single-photon avalanche diode (SPAD) is used along with a time-correlated single-photon counting (TCSPC) module to obtain time resolved measurements. A 75 mm singlet lens is used to image a 3 mm \times 3 mm spot on the wall onto the SPAD pixel. Another galvo is used to steer the imaged spot along the wall. The calibration accuracy of the imaging galvo is also approximately 3 mm. The overall time jitter of the hardware prototype is 64 ps. Data acquisition kits (DAQs) are used to interface the galvos to the PC. Thus, the hardware prototype enables us to capture accurate transients with arbitrary illumination and sensing points on the wall. The specifications of the equipments used is mentioned in Table 1.

Table 1. **Details of the components used to build the hardware prototype.**

Component	Vendor	Part number
Laser	NKT Photonics	EXW-12
Variable band pass filter	NKT Photonics	SuperK Varia
Galvos (\times 2)	Thorlabs	GVS-012
Imaging Lens	Thorlabs	LA1257
SPAD	Micro Photon Devices	PDM
TCSPC Module	PicoQuant	PicoHarp 300
DAQ (\times 2)	NI	USB-6002 & myDAQ
Calibration Camera	FLIR	FL3-U3-13E4M

3.1. System calibration

We calibrate the LOS wall coordinate system with a standard intensity camera looking at the wall. We capture multiple images by placing a checkerboard with known size along the plane of the wall in different orientations and locations. Then

we use MATLAB’s computer vision toolbox to learn the intrinsic, extrinsic and radial distortion parameters of the camera from this set of images. This provides us a mapping from the wall coordinate system to the camera pixels.

To calibrate the illumination galvo, we project laser spots on the wall by varying the voltages applied to the x and y axis mirrors in a grid fashion and capture the wall image for each projected spot. We use the learnt wall-to-camera mapping to obtain wall coordinates for all the projected spots. Then we use the procedure described in [2] to calibrate the galvo voltages with respect to the wall coordinates.

To calibrate the imaging galvo, we similarly image points on the wall by varying the galvo voltages in a grid fashion. However, we cannot capture the spot imaged on the wall directly with the camera. Thus, we instead measure the number of direct bounce photon captured by running the SPAD in free-running mode. For each imaged spot, we sweep the laser spot across the wall and determine the location which maximizes the photon count. This procedure provides us the wall coordinates for each imaging spot and we then use procedure in [2] to calibrate the galvo.

3.2. Real data acquisition

We operate the SPAD in gated mode to remove the contribution of light paths reaching the detector after direct bounce from the LOS wall. Moreover, when an illumination point and a sensing point are exactly co-located, SPAD exhibits artifacts due the direct light paths even in gated mode. Hence, we add a slight offset of $(-2\text{ mm}, -2\text{ mm})$ to the sensing point location desired to be scanned. The acquisition time of transients for a particular illumination/sensing point pair is set to 2s. The size of the calibrated LOS wall is $1\text{ m} \times 1\text{ m}$. With this hardware setup, we acquire confocal transients with uniform grid of 51×51 co-located locations on the LOS wall. The dataset would be made publicly available on the acceptance of this manuscript.

4. Supplementary Results

We provide supports of the results in the main paper, and show additional results.

4.1. Algorithmic implementation details

All algorithms were implemented in MATLAB on Intel Xeon CPU E5-2640 v4 2.40GHz, and convolutions were implemented by FFT on a single GPU (NVIDIA Titan Xp) via inbuilt routines in MATLAB. All timings reported are end-to-end time on MATLAB.

4.2. Scene parameters

The parameters for each scene in the main paper are shown in Table 2. Distance is measured from LOS wall to the center of the reconstruction area. Some datasets such as USAF are downsampled by a factor of two from the original dataset as shown in the time resolution column in the table. The results shown in main paper are smaller than the reconstruction volume because they are cropped for better visualization.

Table 2. Scene parameters.

Figure	Scene	Scanning area (LOS)	Reconstruction volume (NLOS)	Distance	Illumination points	Sensing points	Time resolution	Dataset
Figure 4	S-shape	$1.0\text{ m} \times 1.0\text{ m}$	$0.25\text{ m} \times 0.25\text{ m} \times 0.25\text{ m}$	1.50 m	16×16	16×16	16.0 ps	Simulation (ours)
	USAF	$0.6\text{ m} \times 0.6\text{ m}$	$0.60\text{ m} \times 0.60\text{ m} \times 0.60\text{ m}$	0.50 m	16×16	16×16	33.3 ps	Simulation [3]
	Soap	$0.5\text{ m} \times 0.5\text{ m}$	$0.50\text{ m} \times 0.50\text{ m} \times 0.25\text{ m}$	0.34 m	64×64 (confocal)		8.0 ps	Simulation (ours)
Figure 5	Bunny	$0.5\text{ m} \times 0.5\text{ m}$	$0.50\text{ m} \times 0.50\text{ m} \times 0.25\text{ m}$	0.40 m	64×64 (confocal)		16.0 ps	Simulation (ours)
Figure 6	2019	$1.0\text{ m} \times 1.0\text{ m}$	$1.00\text{ m} \times 1.00\text{ m} \times 1.00\text{ m}$	1.08 m	51×51 (confocal)		64.0 ps	Real (ours)
Figure 7	34	$0.79\text{ m} \times 0.79\text{ m}$	$0.79\text{ m} \times 0.79\text{ m} \times 0.39\text{ m}$	0.51 m	64×64 (confocal)		16.0 ps	Real (ours)
	TX	$1.0\text{ m} \times 1.0\text{ m}$	$0.77\text{ m} \times 0.77\text{ m} \times 0.77\text{ m}$	1.08 m	51×51 (confocal)		64.0 ps	Real (ours)
	Toy	$1.0\text{ m} \times 1.0\text{ m}$	$1.00\text{ m} \times 1.00\text{ m} \times 1.00\text{ m}$	1.08 m	26×26 (confocal)		64.0 ps	Real (ours)

In all experiment, we set the size of voxel to the length of a time bin and used rank-1 kernel only, which we think a sweet spot between algorithm running time and reconstruction quality.

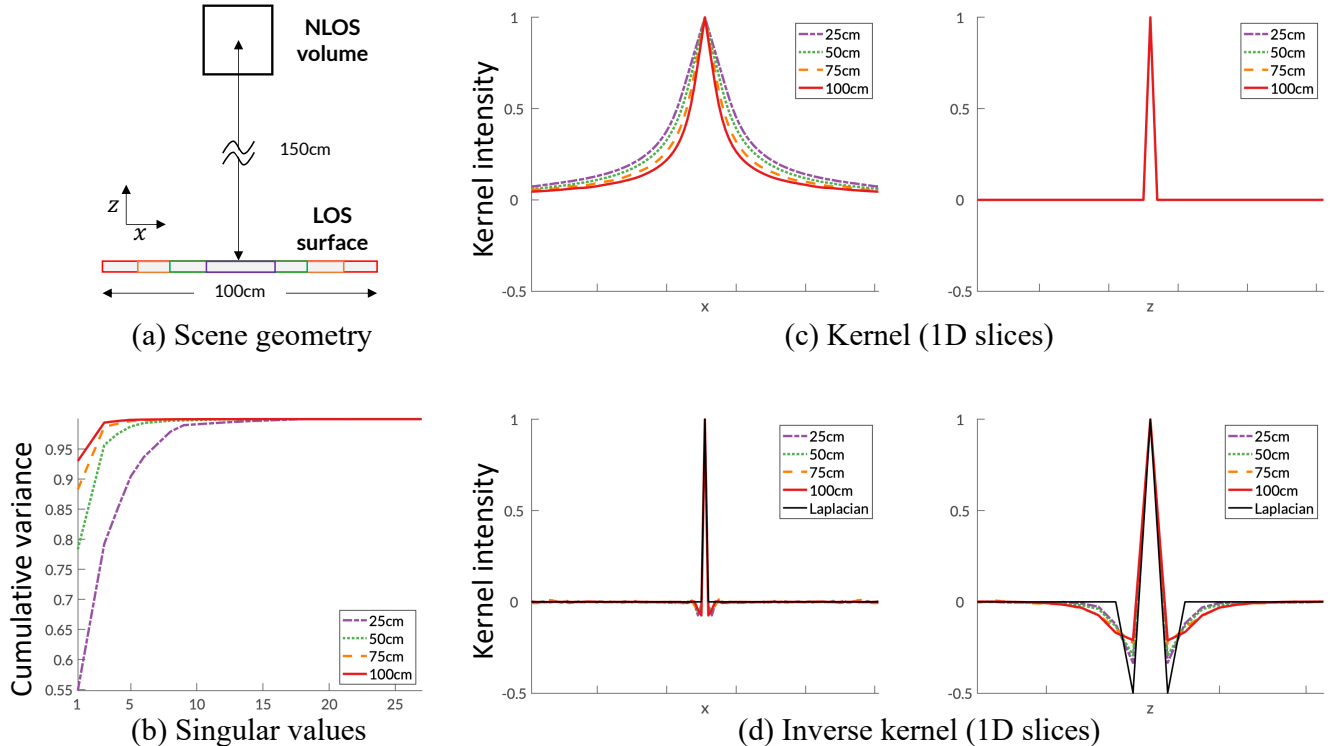


Figure 4. **Validation of rank-1 approximation for a finite LOS surface.** We provide the rank-1 kernel and its SVD result for various size of LOS surfaces. The basic scene geometry is the same as Figure 4(a) in the main paper with LOS surface size $100\text{ cm} \times 100\text{ cm}$. (a) We tested the LOS surface size of 25 cm, 50 cm, 75 cm and 100 cm. (b) The distributions of singular values for various LOS surface size are illustrated. Spatially-varying kernel is well approximated by top eigenvector corresponding to the top singular value, especially when LOS surface is relatively larger compared to NLOS volume, which validates the rank-1 approximation. (c) The shape of kernel is different according to the size of LOS surfaces. (d) The shape of inverse kernel is different according to the size of LOS surfaces, thereby the Laplacian filter, that does not incorporate the effect of LOS surface size, turns out to be suboptimal.

4.3. Rank-1 approximation for a finite LOS surface.

When the assumptions of Proposition 1 are violated, *e.g.*, the LOS surface is not infinite, the blur kernel is spatially-varying, and therefore the Gram operator is not convolutional. However, for cases where the part of NLOS scene occupied by objects is relatively small compared to the LOS surface, we expect that the spatially-varying kernel can still be well approximated by a single convolutional operator.

We demonstrate this empirically in Figure 4: First, we simulate the value of the spatially-varying kernel k for multiple reference points. Then, we perform a singular value decomposition of the simulated Gram matrix, and plot the distribution of the singular values. We observe that the resulting Gram matrix can be well-approximated as a matrix of rank one, with the corresponding best rank-1 approximation (Gram of the first singular vector) acting as an approximate spatially-invariant blur kernel. In Figure 4, the kernels are obtained by this procedure for different size of LOS surfaces, *i.e.*, 25 cm, 50 cm, 75 cm and 100 cm. As shown in Figure 4(b), the spatially-varying kernel is well-approximated by the top eigenvector corresponding to the top singular value, validating the use of single convolution with the top eigenvector for a finite LOS surface.

Additionally, as shown in Figure 4(c,d), the shape of kernels become different as to the size of LOS surface shrinks, and thereby the inverse kernel can be significantly different from the Laplacian filter. Unlike filtered backprojection, our approach naturally accommodates for this by using the correct inverse filter.

4.4. Results from full view

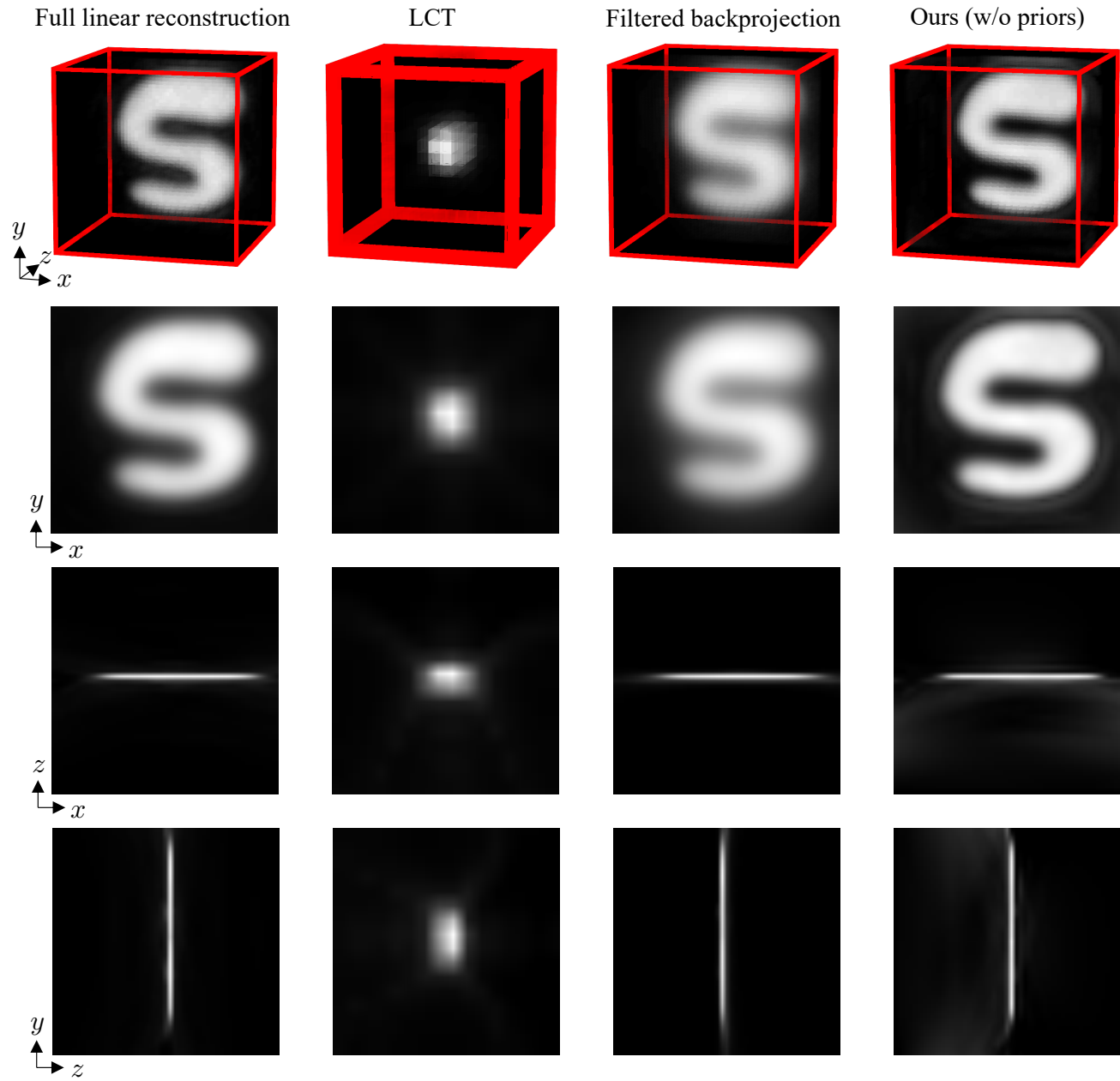


Figure 5. Full results of Figure 4(a) in the main paper.

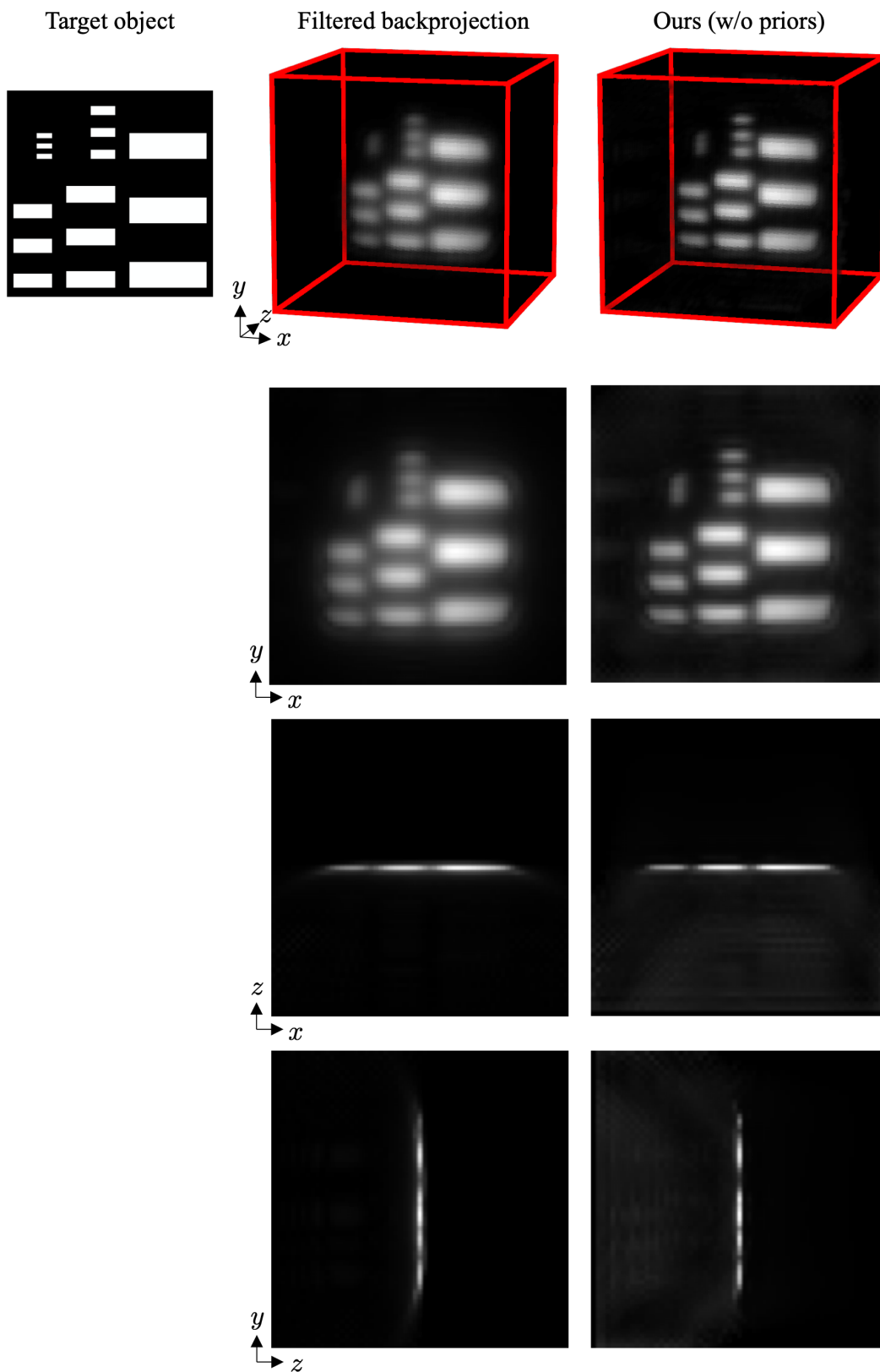


Figure 6. Full results of Figure 4(b) in the main paper.

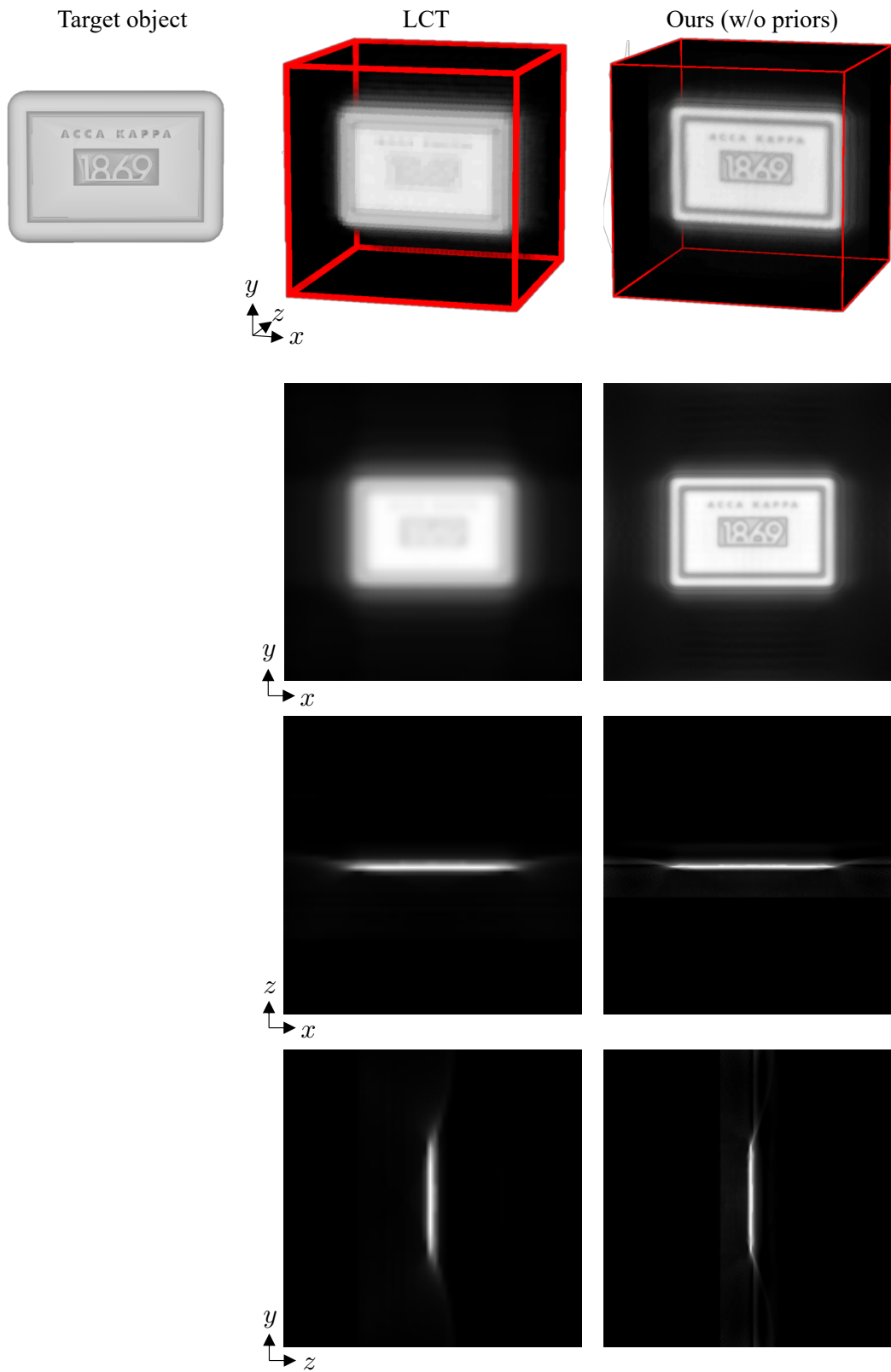


Figure 7. Full results of Figure 4(c) in the main paper.

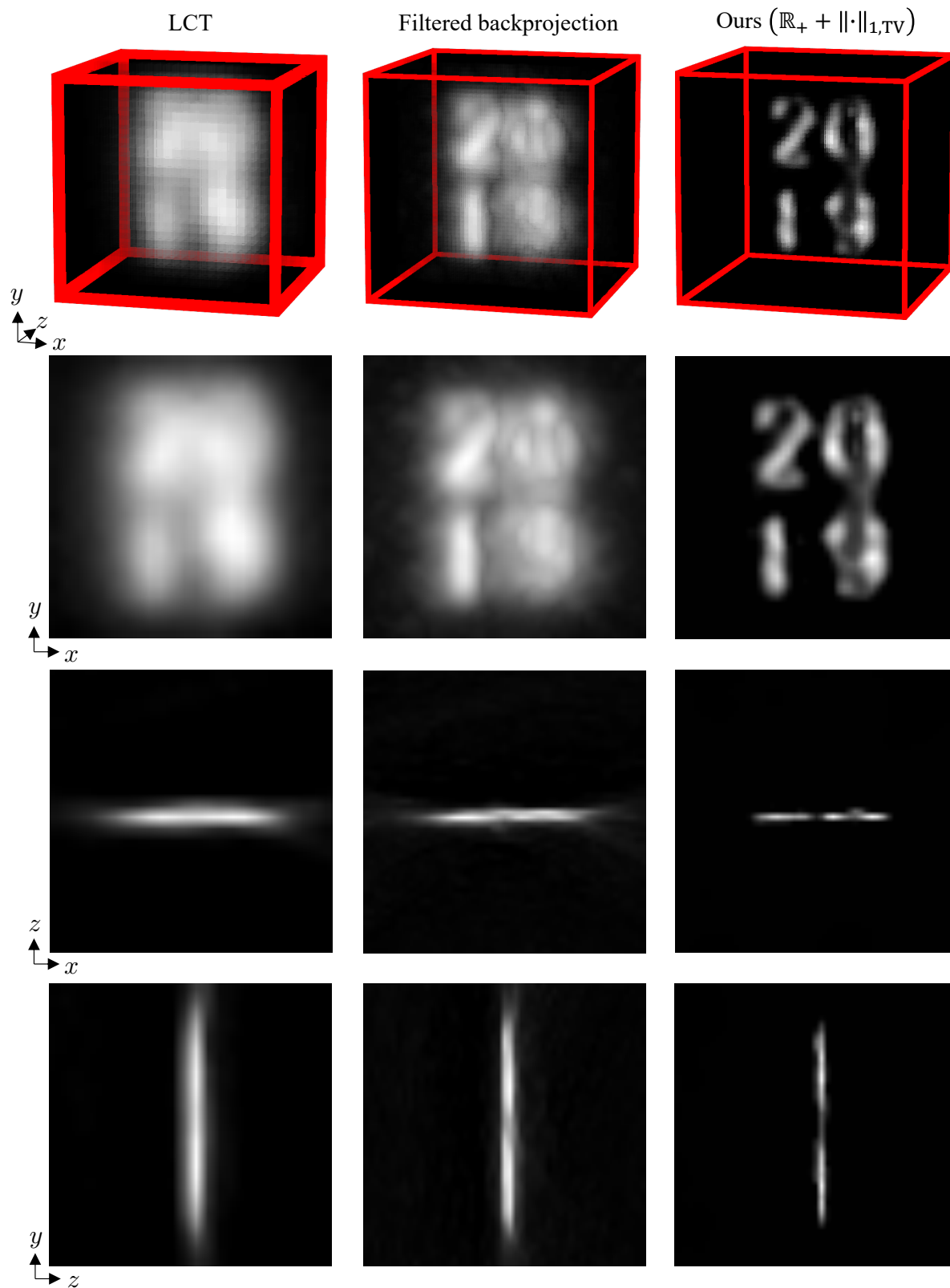


Figure 8. Full results of the third row in Figure 6 in the main paper.

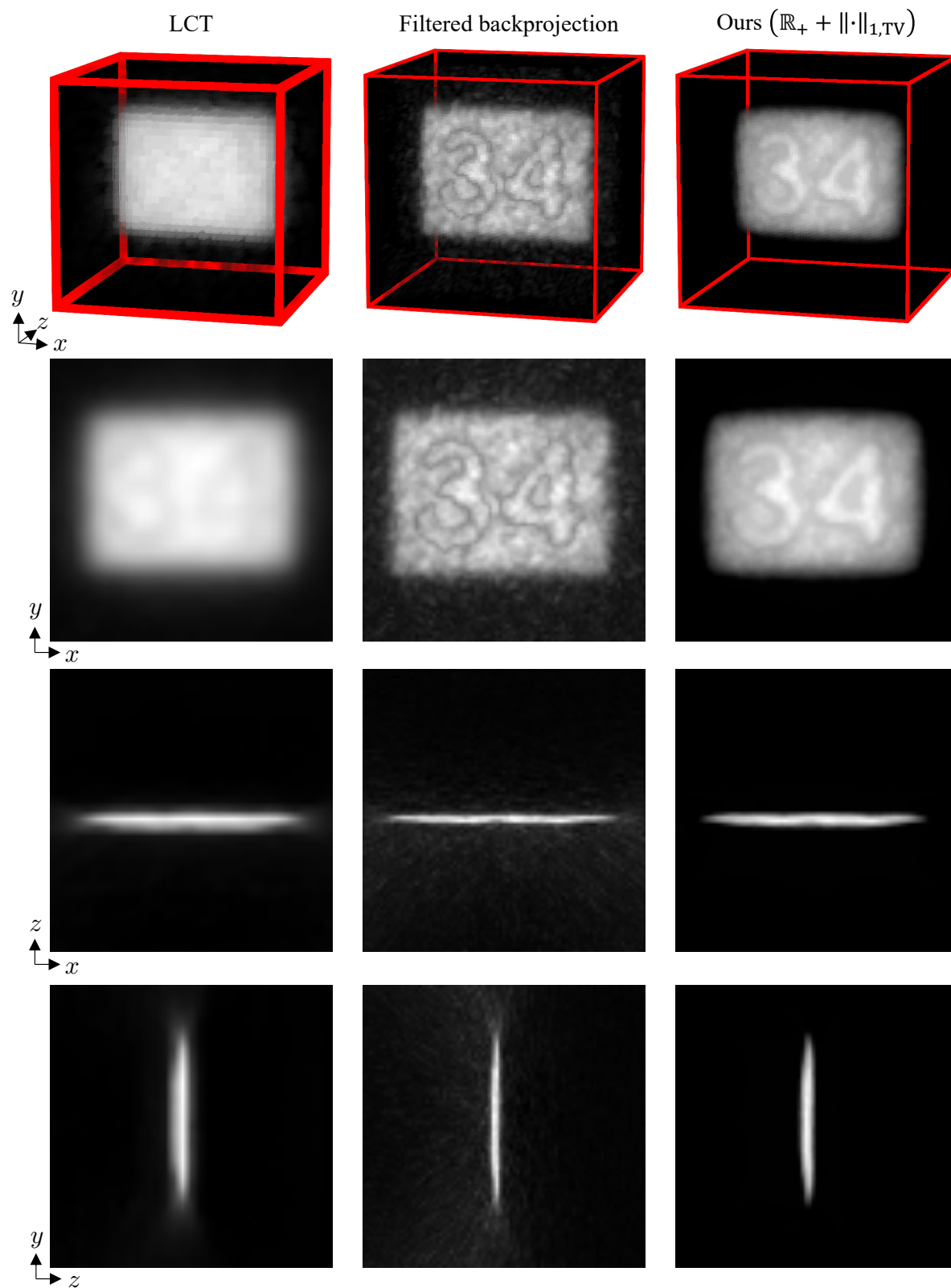


Figure 9. Full results of the first row in Figure 7 in the main paper.

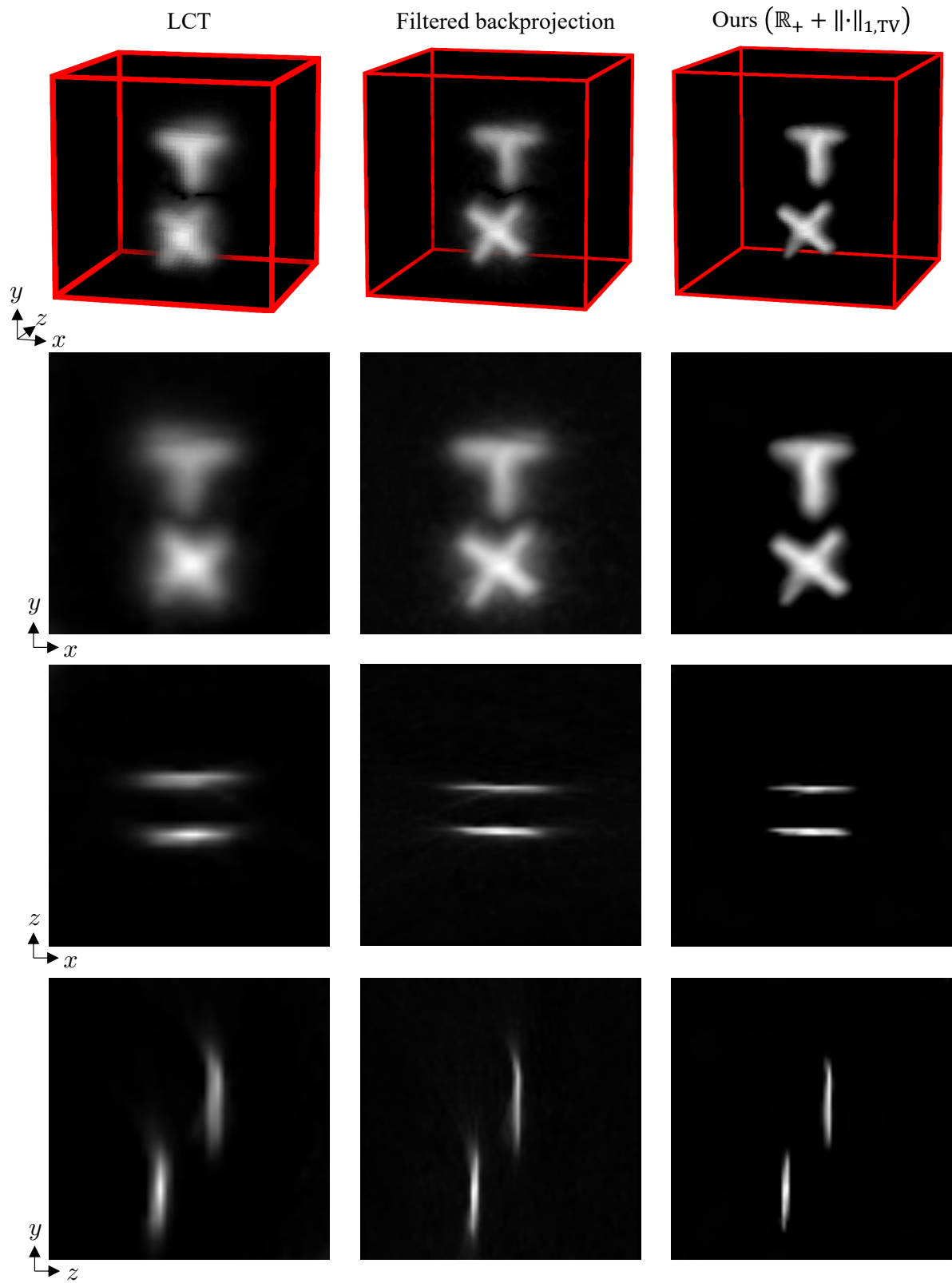


Figure 10. Full results of the second row in Figure 7 in the main paper.

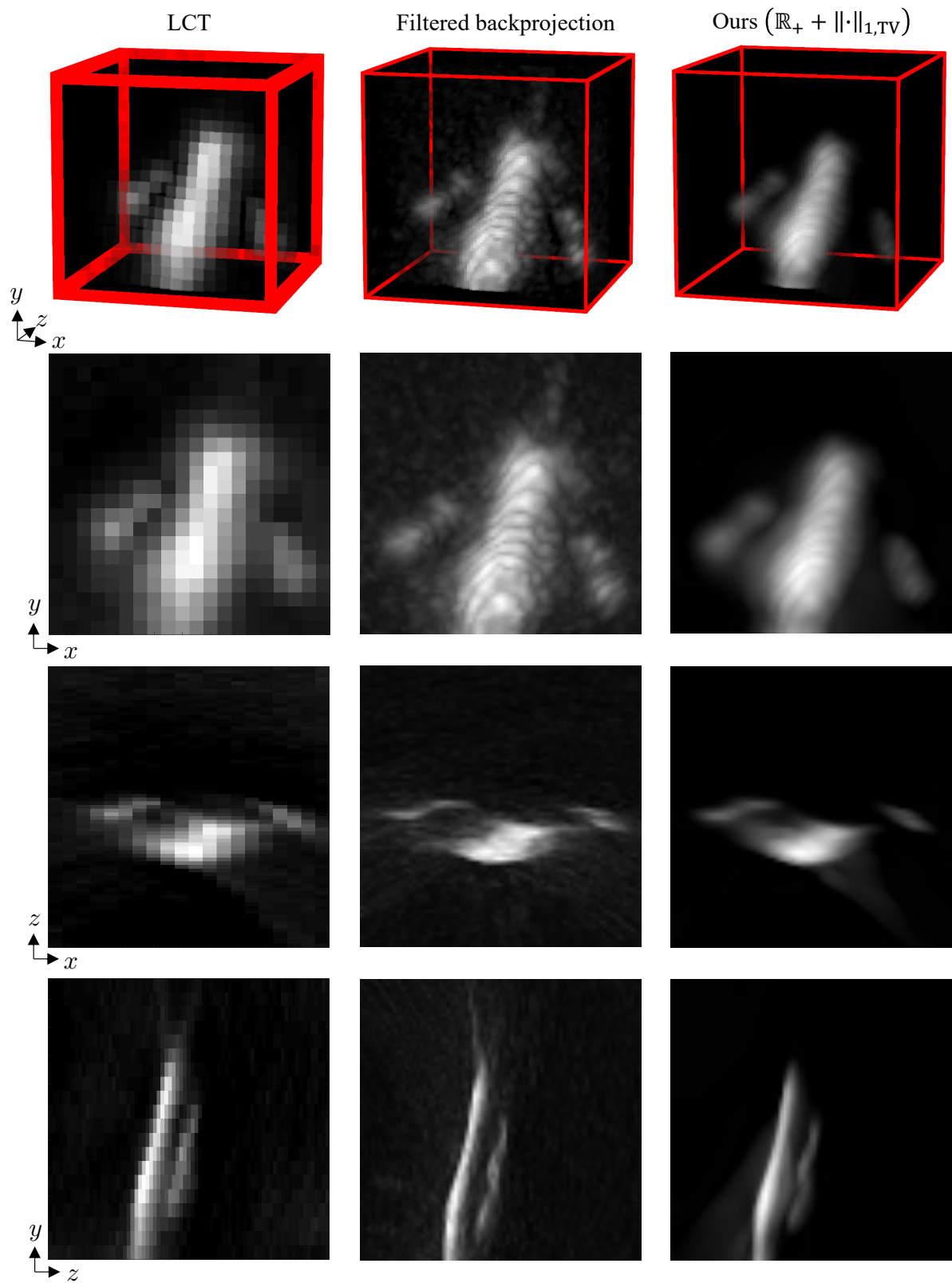


Figure 11. Full results of the third row in Figure 7 in the main paper.

References

- [1] S. Boyd, N. Parikh, E. Chu, B. Peleato, J. Eckstein, et al. Distributed optimization and statistical learning via the alternating direction method of multipliers. *Foundations and Trends® in Machine learning*, 3(1):1–122, 2011. [6](#)
- [2] S. Cui, X. Zhu, W. Wang, and Y. Xie. Calibration of a laser galvanometric scanning system by adapting a camera model. *Applied optics*, 48(14):2632–2637, 2009. [9](#)
- [3] M. Galindo, J. Marco, M. O’Toole, G. Wetzstein, D. Gutierrez, and A. Jarabo. Zaragoza nlos synthetic dataset, 2019. [9](#)
- [4] M. O’Toole, D. B. Lindell, and G. Wetzstein. Confocal non-line-of-sight imaging based on the light-cone transform. *Nature*, 555(7696):338, 2018. [7](#)